Confined in-fiber solidification and structural control of silicon and silicon–germanium microparticles

Alexander Gumennik[a,b,c,1], Etgar C. Levy[a,b,1], Benjamin Grena[a,b,d,1], Chong Hou[a,b,d], Michael Rein[a,b,d,2], Ayman F. Abouraddy[e], John D. Joannopoulos[a,b,f,2], and Yoel Fink[a,b,d]

[a]Research Laboratory of Electronics, Massachusetts Institute of Technology, Cambridge, MA 02139; [b]Institute for Soldier Nanotechnologies, Massachusetts Institute of Technology, Cambridge, MA 02139; [c]Department of Intelligent Systems Engineering, Indiana University Bloomington, Bloomington, IN 47408-2664; [d]Department of Materials Science and Engineering, Massachusetts Institute of Technology, Cambridge, MA 02139; [e]CREOL, The College of Optics and Photonics, University of Central Florida, Orlando, FL 32816; and [f]Department of Physics, Massachusetts Institute of Technology, Cambridge, MA 02139

Contributed by John D. Joannopoulos, May 19, 2017 (sent for review December 9, 2016; reviewed by Ursula Gibson and Max Shtein)

Crystallization of microdroplets of molten alloys could, in principle, present a number of possible morphological outcomes, depending on the symmetry of the propagating solidification front and its velocity, such as axial or spherically symmetric species segregation. However, because of thermal or constitutional supercooling, resulting droplets often only display dendritic morphologies. Here we report on the crystallization of alloyed droplets of controlled micrometer dimensions comprising silicon and germanium, leading to a number of surprising outcomes. We first produce an array of silicon–germanium particles embedded in silica, through capillary breakup of an alloy-core silica-cladding fiber. Heating and subsequent controlled cooling of individual particles with a two-wavelength laser setup allows us to realize two different morphologies, the first being a silicon–germanium compositionally segregated Janus particle oriented with respect to the illumination axis and the second being a sphere made of dendrites of germanium in silicon. Gigapascal-level compressive stresses are measured within pure silicon solidified in silica as a direct consequence of volume-constrained solidification of a material undergoing anomalous expansion. The ability to generate microspheres with controlled morphology and unusual stresses could pave the way toward advanced integrated in-fiber electronic or optoelectronic devices.

multimaterial fibers | microparticles | confined solidification | silicon–germanium spheres | stressed silicon

Controlling the microstructure or state of stress of microparticles and nanoparticles is often key to attaining the desired properties for a specific application (1–5); however, the ability to do so is strongly limited by the synthesis method. For instance, nonspherically symmetric distributions of inorganic materials are difficult to achieve from bottom-up approaches (4–7). Likewise, controlling the state of stress or strain of semiconductor particles is challenging in unconstrained nucleation-and-growth synthesis methods. However, Janus particles of silicon–germanium (SiGe) could potentially find applications as microswimmers or nanoswimmers owing to asymmetric absorption properties (8), as well as in infrared photodetectors or solar cells for increased infrared absorption (9). Stressed silicon particles, on the other hand, could be used for bandgap tunability in photonic or optoelectronic devices (10–12).

In the past few years, thermally drawn multimaterial fibers have emerged as a unique platform for top-down scalable fabrication of microparticles to nanoparticles over a broad range of materials, through controlled in-fiber capillary breakup of the fiber components (13–15). In the case of polymers or chalcogenide glasses, structural control of the particle can be achieved by constructing complex cores at the preform level, which is later broken up in the fiber state to form structured particles (13). However, in the case of traditional semiconductor materials such as silicon and germanium, the same method cannot be applied because of the low viscosity and high solubility of the materials in the molten state (16). As a result, components of the core intermix during fiber drawing or breakup, and the initial core structure is lost. Another route needs to be used to go beyond those limitations.

The solidification of SiGe and pure silicon and germanium has been the subject of a large number of studies in different types of configurations and geometries (16–20). First of all, both the alloy and pure materials are known to expand upon solidification, owing to their diamond cubic structure, such that constrained solidification should be associated with pressure buildup. Second, despite complete solubility of silicon and germanium in both solid and liquid states, the phase diagram of SiGe displays a large miscibility gap, with a higher solubility of germanium in the liquid state (16). At slow enough solidification rates, the initial nuclei are silicon-rich, thereby rejecting germanium into the melt. As solidification proceeds, more and more germanium is rejected into the melt, and a nonuniform distribution of germanium arises because of slow diffusion of solute in the solid phase. Naively, directional solidification of SiGe in a strong thermal gradient could lead to Janus morphologies. However, it is well known that germanium rejection in the liquid tends to create strong compositional gradients driving constitutional supercooling of the alloy, leading to growth of dendritic or cellular morphologies (17, 18, 21–24). Therefore, in practice, stable solidification front propagation and Janus morphologies are difficult to achieve.

Here we show that we can use a flame breakup approach to produce compositionally segregated particles, referred to as Janus particles of SiGe, in a scalable manner. We suppress constitutional

Significance

Water freezing into ice has a number of fascinating outcomes: Dendritic solidification of water results in beautiful snowflakes, a sealed bottle of beer shatters in a freezer, and ice covering salty oceans at the poles is salt-free due to compositional segregation. A silicon–germanium (SiGe) material system, ubiquitous in microelectronics, is surprisingly similar to water in its solidification behavior. Quenching of molten SiGe microdroplets sealed inside a glass fiber leads to dendritic morphology, with potential use in solar cells. Slow cooling induces compression of these spheres to tens of thousands of atmospheres, potentially changing the band structure of these materials. Moreover, slow solidification results in compositionally segregated SiGe Janus particles, useful for high-frequency microelectronic and nanorobotic applications.

Author contributions: A.G., E.C.L., B.G., C.H., A.F.A., and Y.F. designed research; A.G., E.C.L., C.H., and M.R. performed research; A.G., E.C.L., B.G., C.H., M.R., and J.D.J. analyzed data; A.G., E.C.L., B.G., C.H., M.R., and Y.F. wrote the paper; and Y.F. supervised the research.

Reviewers: U.G., Norwegian University of Science and Technology; and M.S., University of Michigan.

The authors declare no conflict of interest.

[1]A.G., E.C.L., and B.G. contributed equally to this work.

[2]To whom correspondence may be addressed. Email: mlrein@mit.edu or joannop@mit.edu.

This article contains supporting information online at www.pnas.org/lookup/suppl/doi:10.1073/pnas.1707778114/-/DCSupplemental.

supercooling by slow feed speeds of the fiber into the flame. We can also recrystallize the particles postbreakup using a combination of a CO_2 and diode laser, enabling accurate control over cooling rate as well the ability to reorient the Janus particles' axis. In addition, confined solidification of silicon leads to hydrostatic pressure buildup in the particles because of the anomalous expansion, which we demonstrate through both birefringence and Raman spectroscopy measurements.

Results

Our general method starts with the fabrication of a fiber consisting of a crystalline semiconductor core surrounded with a silica cladding, through the preform-to-fiber thermal drawing process (14, 25, 26). Here, we focus on cores made of silicon, germanium, or a mixture of both. Once drawn, the fiber is fed at a velocity v_f through a flame that locally heats the core and the cladding above their melting and softening temperatures, respectively, and induces local capillary breakup of the semiconductor core into a liquid droplet surrounded by silica (14), as illustrated in Fig. 1*A*. As the fiber exits the flame, it cools down. Because both silicon and germanium have melting points below the softening point of silica, the cladding hardens first and creates a smooth hermetic spherical vessel surrounding the molten semiconductor droplet. Subsequently, the droplet solidifies in a temperature gradient imposed by the flame, and the solidification front (denoted by ξ in Fig. 1*A*) is expected to propagate from the colder side toward the hotter side, in the absence of constitutional supercooling.

We have experimentally demonstrated lateral solidification of SiGe droplets by fabricating an array of axially oriented SiGe Janus particles from a $Si_{0.5}Ge_{0.5}$ core fiber (Fig. 1*A*). Backscattered Mode Scanning Electron Microscopy (SEM) and Energy Dispersive Spectroscopy (EDS) mapping of the fabricated $Si_{0.5}Ge_{0.5}$ spheres suggest that the SiGe distribution has a distinct axial dependence, oriented along the fiber axis (Fig. 1 *B*–*D*). The SiGe map in Fig. 1*D* clearly shows that the sphere is a Janus particle having a Si-rich lobe and a Ge-rich lobe. The quantitative analysis of EDS shows that the Si:Ge ratio in the Si-rich lobe is roughly 5:2 (Fig. 1*F*), similar, yet not identical, to what is expected from the respective isothermal quasi-static segregation coefficient for $Si_{0.5}Ge_{0.5}$ melt resulting from the SiGe phase diagram (16) (Fig. 1*E*). A detailed theoretical derivation of the Ge and Si redistribution in the solid sphere is given in *SI Analytical Derivation for the Ge Content Distribution in the Solid Phase* and Fig. S1, where we assume that the solidification front remains stable and propagates axially. A good agreement is found between experimental and theoretical composition distributions (Fig. 1*F*).

The discrepancy between the model and the data noticeable in the Si-rich lobe can be explained by the fact that the initial solidification occurs through fast dendritic growth as opposed to slow and stable solidification, which our model assumes. We assume the unstable growth of the initial transient regime to be governed by both thermal and constitutional supercooling. As solidification proceeds in the confined droplet, both mechanisms for instability will lose magnitude. Indeed, the release of latent heat from partial solidification can lead to the temperature in the liquid increasing close to the melting point of the alloy—a phenomenon known as recalescence (27, 28)—by definition reducing thermal undercooling. Second, because of the finite volume, rejection of germanium from the solid gradually decreases the silicon content in the liquid region, which is expected to suppress constitutional supercooling by effectively increasing the critical velocity (29).

Clearly, the stability of the solidification front propagation is a requirement to obtain axial germanium distribution. If cooling conditions were such that the solidification front in the droplet was indeed unstable throughout the sphere volume, the resulting spheres would likely display cellular or dendritic microstructures

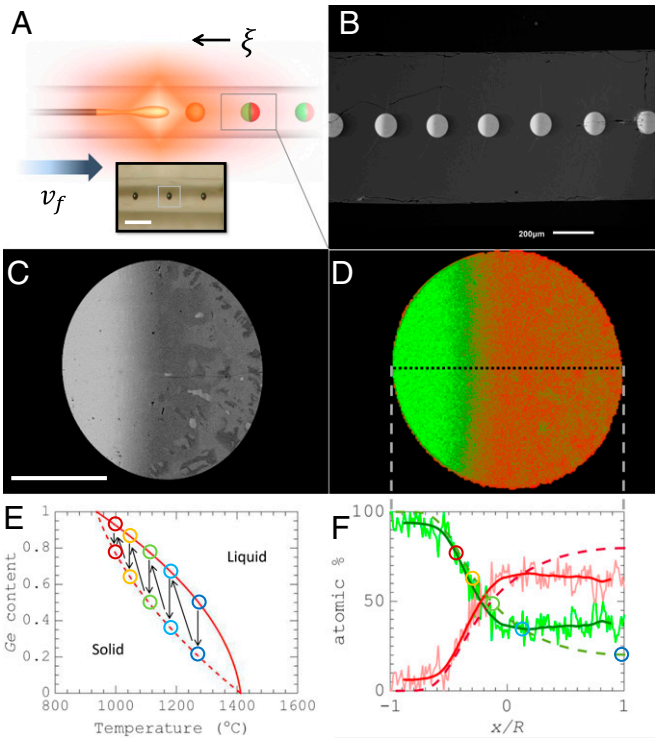

Fig. 1. $Si_{0.5}Ge_{0.5}$ heterostructured cellular composition structure particle fabrication. (*A*) Schematics of fabrication process of the Janus particles array. (*Inset*) The generated SiGe spheres within the silica fiber. (Scale bar, 500 μm.) (*B*) SEM measurement in backscattered mode of the polished fiber along its axis showing a fiber-embedded array of Janus particles. (*C*) A single sphere cross-section SEM backscattered mode measurement. Brighter areas correspond to a higher Ge concentration. Traces of an unstable liquid–solid interface during the beginning of the crystallization are observed on the right side of the sphere, and gradual distribution is observed from the middle of the sphere to its left side. (Scale bar, 50 μm.) (*D*) SiGe ratio EDS map of the median cross-section of a $Si_{0.5}Ge_{0.5}$ sphere embedded in a silica fiber, resulting from overlaid maps of Si (in red) and Ge (in green). (*E*) The SiGe equilibrium phase diagram: the liquidus (solid line) and the solidus (dashed line) are described. The process of the Ge rejection during the solidification of a $Si_{0.5}Ge_{0.5}$ binary alloy is schematically described: The solidification starts at about the point (50%Ge, 1,287 °C), marked by a blue circle on the liquidus, and the solidification is described by the vertical arrow to the point (20%Ge, 1,287 °C), marked by a blue circle on the solidus (dashed line). As the solidification propagates, Ge is rejected to the liquid phase, and the Ge content in the melt increases while the melting temperature decreases. The resulting increase of the Ge content in the liquid phase due to the solidification is described by the diagonal arrow from the blue circle on the solidus to the cyan circle in the liquidus. As the isothermal solidification propagates, the Ge content in the melt approaches unity, and the melting temperature approaches that of a pure Ge. (*F*) The graph depicts SiGe atomic content distribution along the dashed line in *D*. The solid light green/red lines correspond to a single pixel linescan, that is, a 0.7-μm-wide analysis area. The solid dark green/red lines correspond to the same linescan with a 14.7-μm-wide analysis area, and are calculated by having the 2D image in *D* filtered using a 10-pixel-radius disk. The measured data are overlaid with the theoretical result calculated from the solidification front propagation (dashed red/green). The expected Si and Ge concentration along the sphere median is calculated assuming that the solidification front remains stable and propagates axially. The data were extracted along the dotted line that is described in *D*. For each circle on the theoretically calculated spatial Ge content distribution (green dashed line), there is a corresponding circle with the same color on the solidus line described in *E*, such that the spatial *x* coordinate of the sphere can be associated with the corresponding solidification temperature via the Ge content. The process results in Janus particles, one lobe of which is 5:2 of Si:Ge, and the other is Ge, with a boundary about 20 μm wide between them.

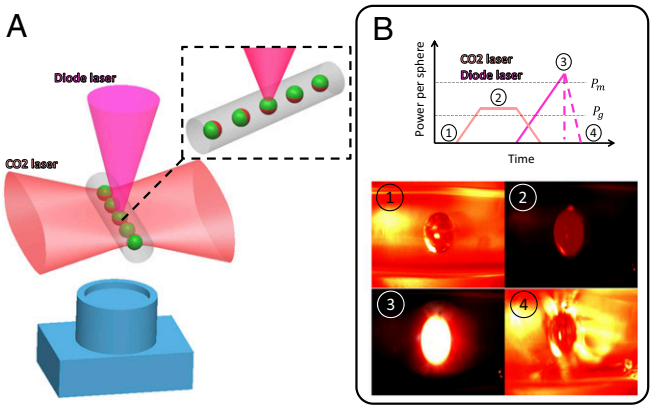

Fig. 2. Laser-induced solidification experimental setup. (*A*) Schematic description of the experimental setup, consisting of a diode laser beam at 808 nm and two CO_2 laser beams at 10.6 μm. The silica cladding of the fiber is transparent at the diode laser wavelength but absorbs in the CO_2 wavelength. This experimental setup enables control over the initial sphere temperature and its cooling rate. (*Inset*) The particle axis reorientation by the laser. (*B*) (*Top*) Schematic description of the heating and cooling processes of each sphere. The CO_2 preheating stage is used to prevent cracks during the sphere heating by preheating and softening the silica cladding first. The power thresholds for the silica softening by the CO_2 laser and for the sphere melting by the diode laser are represented by P_g and P_m, respectively. (*Bottom*) Images of the sphere during the stages described by the graph, showing the sphere before the experiment (*1*), during the preheating of the silica (*2*) followed by the main heating of the sphere (*3*), and after the sphere temperature decreases back to the room temperature (*4*).

with no particular orientation (17, 18, 20, 30). Despite promising results, the flame setup does not allow sufficient control over the cooling kinetics and thermal gradient direction, and we have therefore used a technique of laser-induced recrystallization, allowing us to not only study more precisely the effect of the cooling conditions but also control the axis of the Janus particle within the fiber. A similar setup was recently used by Coucheron et al. (20) to control the microstructure of SiGe core fibers.

Here, a postbreakup particle is illuminated perpendicularly to the fiber axis by a focused diode laser beam at a wavelength of 808 nm, with a spot size of about 50 μm. To prevent the cracking of the cladding, which might occur as a result of the release of stresses stored in the silica cladding, we uniformly preheat and soften it with a CO_2 laser (Fig. 2*A*). The absorption length of silica and silicon at 808 nm is about 1.5 m and 12.5 μm, respectively. Therefore, the diode laser radiation is expected to be transmitted by the silica cladding but to be absorbed by the particle, which heats up. Once the particle is molten, the laser power is gradually reduced and the particle cools down and recrystallizes, while exposed to a thermal gradient defined by the diode laser direction. The process is schematically represented in Fig. 2*B*. By controlling the laser shut-off rate, we can effectively control the cooling conditions and the magnitude of the imposed temperature gradient.

We have recrystallized spheres of $Si_{0.75}Ge_{0.25}$ and $Si_{0.95}Ge_{0.05}$ under different laser shut-off rates, as shown in Fig. 3. Spheres recrystallized by abrupt laser diode shut-off led preferentially to cellular structures with no axial distribution, whereas spheres recrystallized at low shut-off rates displayed Janus morphologies aligned along the diode laser direction. We can therefore dictate the microstructure of SiGe particles by controlling the shut-off rate of the laser, as well as reorient the axis of the Janus particles by choosing the diode laser direction. Furthermore, we noticed apparent striations in the germanium concentration for $Si_{0.95}Ge_{0.05}$ samples, with a periodicity around 15 μm. Such fluctuations are common in the growth of SiGe from both Czochralski and Bridgman processes (31–33). Generally these striations show a 10- to 15-μm periodicity independent of growth conditions, and commonly attributed to fluctuations in growth velocity associated with time-dependent temperature fluctuations at the interface that can be due to convection or fluctuations in solid-phase conductivity (31–33). Here we believe a similar mechanism is at play.

To explain the overall microstructures' dependence on the laser shut-off rate, we need to understand what affects the constitutional supercooling of SiGe in our solidifying droplets. In general, constitutional supercooling arises when solute rejection in the liquid creates steep concentration gradients near the solidification front, leading to a situation where the actual temperature ahead of the front is lower than the liquidus temperature near the interface, which drives instability (29, 34). This concentration profile occurs if the diffusion of solute in the liquid is slow compared with the solidification velocity, thus resulting in strong gradients at the interface. Hence qualitatively slow shut-off rates would lead to slower solidification and a higher chance of suppressing constitutional supercooling, which is consistent with the observations. Tiller et al. (21) developed a model to compute a critical solidification front velocity above which a binary alloy will develop constitutional supercooling. Later, Mullins and Sekerka (22) enriched the model to take into account effects of interfacial tension and thermal conductivity differences. However, these models only deal with solidification of alloys with no boundaries. Here our system is a confined droplet in thermal contact with a silica cladding, for which most of the Tiller et al. and Mullins and Sekerka assumptions fall short.

Therefore, we have taken a semiquantitative approach instead, to try to predict the outcome as a function of the laser shut-off rate in our specific geometry. We used numerical simulations to estimate the temperature field and solidification front velocity for different shut-off rates in a pure silicon droplet, and

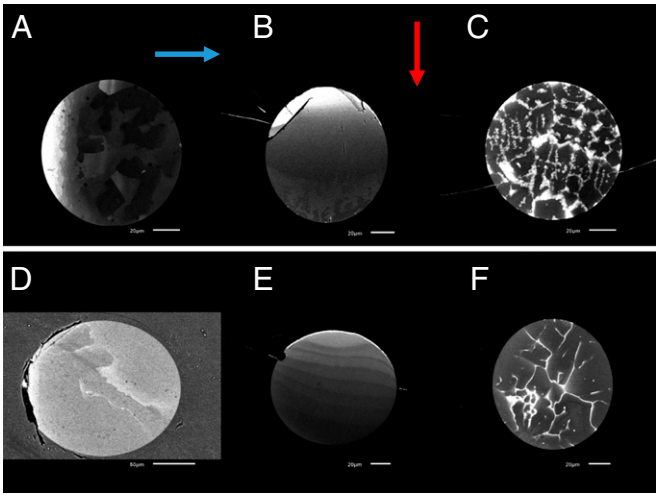

Fig. 3. Controlling the structure of SiGe microspheres. (*A* and *D*) Flame-induced and (*B* and *E*) laser- induced stable solid–liquid interface solidification of (*A* and *B*) $Si_{0.75}Ge_{0.25}$ and (*D* and *E*) $Si_{0.95}Ge_{0.05}$ binary alloy microspheres. The blue and the red arrows show the fiber movement direction through the flame in *A* and the laser iluminlation direction in *B*, respectively. The fiber velocity was 10 μm/s. The monotonic Ge distribution that is observed in the top regions of spheres in *B* and *E* is consistent with a stable liquid–solid interface during the solidification front propagation, after the initial dendritic transient regime. The cooling rates in the results in *B* and *E* were 0.04 W/s and 3 W/s, respectively. (*C* and *F*) The cellular sphere morphology structure when the laser intensity was shut off abruptly; the cooling rate is dominated by heat diffusion rate from the sphere to the environment. The initial laser intensitities in the results presented in *B*, *C*, *E*, and *F* were 2.6 W, 2 W, 1.8 W, and 2 W, respectively.

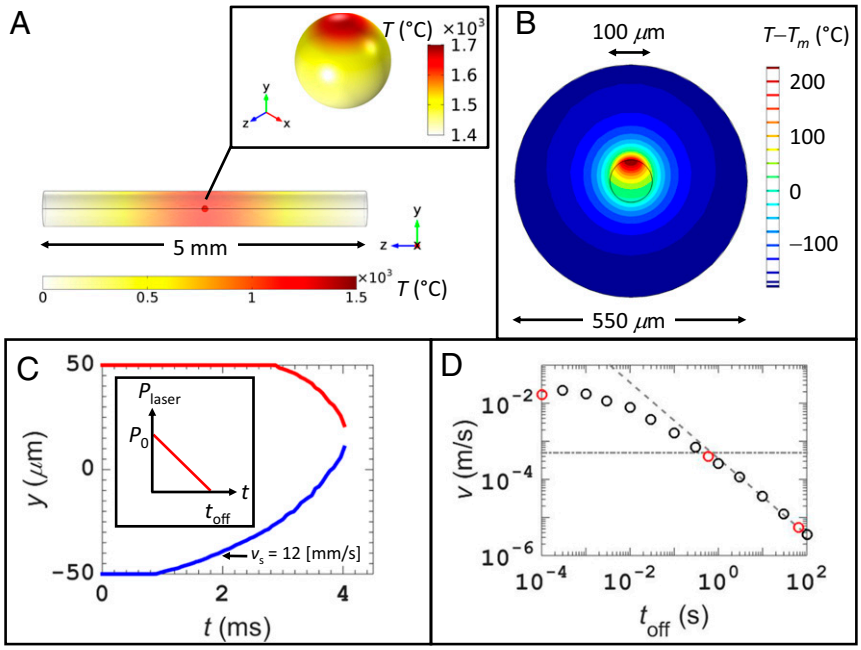

Fig. 4. Theoretical computation of the solidification front propagation velocity. (*A*) The calculated steady-state temperature of the 3D geometry that was modeled: a 100-μm-diameter Si sphere, encapsulated within a 550-μm-diameter silica fiber section of 5 mm. The sphere center coincides with the axis origin. A heat source condition was set in the sphere domain to simulate the absorption of $P_0 = 2$ W intensity radiation focused on a 50-μm-diameter spot, wavelength of 808 nm and directed in the $-y$ direction. (*Inset*) The temperature of the entire sphere is above the Si melting temperature. (*B*) The temperature of a cross-section along the sphere center. (*C*) The solidification front propagation as a function of time along the line ($x = 0$, $y,z = 0$). The solidification front propagation is a result of a time-dependent calculation, in which the steady-state solution that is described in *A* and *B* is set as the initial condition, and in which the heat source intensity decreases linearly from $P_0 = 2$ W to 0 during a shut-off time $t_{off} = 3$ ms (*Inset*). The initial solidification front propagation velocity equals 12 mm/s. (*D*) The calculated dependence of the solidification front propagation velocity on the shut-off time (circles). The dashed line is given by $v = 7 \cdot R_S / t_{off}$, where R_S is the sphere radius. The dash-dotted line corresponds to the effective diffusion velocity and is given by $v = D/R_S$, where $D = 2.5 \cdot 10^{-8}$ m^2/s is equal to the diffusion coefficient of Ge in Si (41). The red marked circles correspond to cooling rates of $2 \cdot 10^4$ W/s, 3 W/s (similar to the cooling rate that was obtained in Fig. 3*E*), and 0.04 W/s (similar to the cooling rate that was obtained in Fig. 3*B*).

compared them with the estimated germanium diffusion rate in the melt from a scaling argument (Fig. 4). A detailed description of the numerical simulations is presented in *SI Numerical Simulation of the Solidification Front Propagation Velocity* and Table S1. As expected from our discussion, slow cooling leads to much slower solidification than diffusion and, consequently, to a stable nonsupercooled solidification. On the other hand, rapid laser shut-off (shut-off time less than 10 ms) causes the solidification rate to exceed the germanium diffusion rate, which would promote constitutional supercooling (34). In both cases, the experimental results are consistent with the predicted behaviors.

Our qualitative model has several shortcomings. Namely, we perform the thermal simulation for a droplet of pure silicon. A more realistic approach should take into account the germanium content, which affects the thermal properties of the solid and liquid phases, the latent heat, and the freezing point of the liquid. We expect that the solidification front velocity will be affected, and likely will decrease as the liquid freezing point decreases at higher germanium content for a given set of external cooling conditions, thereby, in fact, promoting stability due to the confinement.

The in-fiber confined solidification of particles has interesting consequences not only for the morphologies of SiGe alloys but also for their stress state. The presence of stress was indicated by cracks in thin-cladding fibers systematically appearing in the silica surrounding individual particles after solidification of the droplets (see *SI Cracked Fiber Due to Stress Buildup* and Fig. S3). As mentioned, both SiGe and pure silicon and germanium expand upon solidification. When the postbreakup droplets reach the solidification temperature, they are restricted to their liquid volume by the relatively stiff surrounding silica cladding. The anomalous expansion upon solidification thus causes the droplets to strain the surrounding silica and to develop internal compressive stress (Fig. 5*A*), much like a water bottle in the freezer. We studied this effect in pure silicon to avoid complexities arising from nonuniform germanium distribution such as nonuniform volume expansions. Assuming a state of uniform stress in the spheres, we can compute its magnitude. The detailed calculation can be found in *SI Homogeneous Solidification Scenario* and Fig. S2, and it leads to a uniform hydrostatic stress of 2.9 GPa in solidified silicon droplets, independent of their diameter. These calculations do not take into account any possible plastic deformation of the silica cladding, which would limit the magnitude of the stresses.

The resulting strain in silica can also be quantified optically through a photoelastic measurement. The strain field in silica alters its refractive index and causes the material to become birefringent, which we can observe using cross-polarizers (Fig. 5*C*). Contrary to the region around the spheres, the intact section of the core remains unstressed (refer to *SI Evaluation of Stress in the Silica Cladding Surrounding the Sphere by Crossed Polarizers Technique*, Figs. S4–S7, and Table S2 for details). The birefringence pattern around the spheres displays a fourth-order rotational symmetry as well as multiple Michel–Levi rings (35) (Fig. 5*D*). By taking into account the photoelastic coefficients of silica, we can compute the expected birefringence patterns for arbitrary stresses at the silica/semiconductor interface (see *SI Evaluation of Stress in the Silica Cladding Surrounding the Sphere by Crossed Polarizers Technique*, Figs. S4–S7, and Table S2 for details of the calculations) and evaluate the surface stress by matching the number of rings with the experimental patterns (Fig. 5*E*). This method enables us to define the range of surface stresses coherent with a given number of rings. For a 35-μm-diameter Si droplet, the surface stresses were

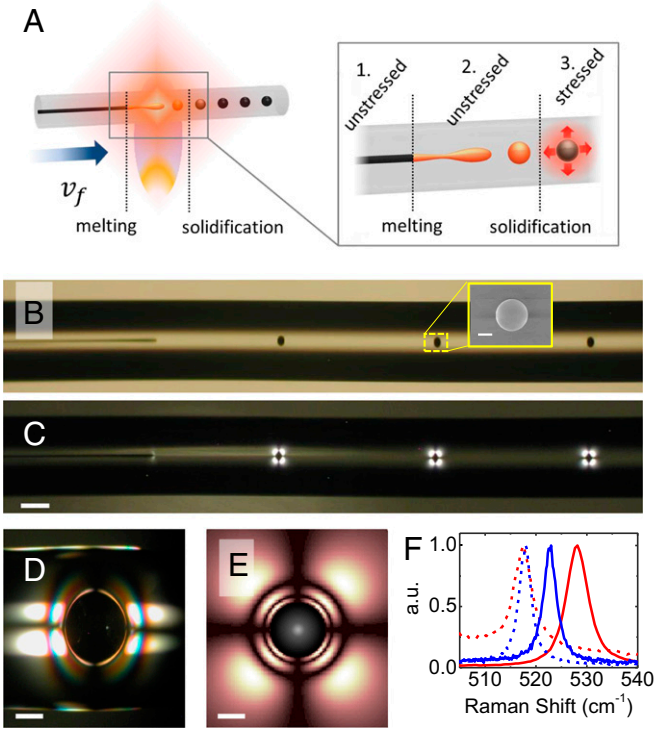

Fig. 5. Basic concept of stress development. (*A*) Schematics of breakup (*Left*), and evolution of aggregation and stress conditions of the breaking-up core material (*Right*): (*1*) Premelted core is solid. (*2*) The core melts into liquid while entering the hot zone. (*3*) The liquid material thread breaks up into spheres encapsulated in silica, which expand upon solidification while leaving the hot zone. (*B*) A section of the fiber resulting from the process in *A*, including a continuous core followed by broken-up spheres as observed under a transmission optical microscope. (*Inset*) A SEM image of an individual 35-μm-diameter sphere after being released from the silica cladding by dissolution in hydrofluoric acid. On the optical image, the spheres visually appear to be elongated perpendicularly to the fiber axis. This optical effect is due to the curved silica cladding, acting as cylindrical lens and distorting the image accordingly. The actual particle is in fact spherically symmetric, as is shown by the SEM image (*Inset*). (Scale bar, 15 μm.) (*C*) Same as *B*, while placed between crossed polarizers. Azimuthally fourfold stress fields in the silica surrounding the spheres are clearly evident. Absence of stresses in the continuous core region is evident as well. (Scale bar, 100 μm.) (*D*) Stress pattern around the 450-μm Si sphere as observed in cross-polarizing setup. (Scale bar, 200 μm.) (*E*) The calculated (*SI Evaluation of Stress in the Silica Cladding Surrounding the Sphere by Crossed Polarizers Technique*, Figs. S4–S7, and Table S2) stress pattern as would be observed in the cross-polarizing setup assuming the radial surface stress in the silica of 0.218 GPa for the Si sphere of the same dimensions as the one in *D*. (Scale bar, 200 μm.) (*F*) Raman shift in the prebreakup continuous core sections of the samples in *B* (dashed red) and *D* (dashed blue) compared with those of the postbreakup spheres in *B* (solid red) and *D* (solid blue). The core–sphere changes in Raman shifts for 35-μm and for 450-μm spheres are 10.5 ± 0.2 cm^{-1} and 4.7 ± 0.1 cm^{-1}, respectively.

between 0 GPa and 0.9 GPa, whereas, for a 450-μm-diameter Si droplet, the surface stresses lay between 0.15 GPa and 0.22 GPa. Although consistent with a state of high internal stress, the measurements lacks precision, and the values differ quite significantly from the theoretically derived stress. The discrepancy between the stress values may be due to plastic deformation occurring in the silica cladding at the relatively elevated temperature at which the deformation is taking place (~1,000 °C).

We decided to evaluate stress through an alternative method, by performing Raman spectroscopy using a 78-nm-wavelength laser on silicon spheres and comparing the results with continuous core sections. For hydrostatically stressed silicon, the shift of the first-order Raman peak frequency ω depends on the pressure P according to $d\omega/dP = 5/2 \pm 0.3$ cm^{-1} per gigapascal (36). Raman measurements on the 35- and 450-μm-diameter Si droplet indicate a shift in the silicon peak location of 10.5 ± 0.2 cm^{-1} and 4.7 ± 0.1 cm^{-1}, respectively (Fig. 5*F*). These shifts translate into hydrostatic stresses of 2.02 ± 0.07 GPa and 0.90 ± 0.06 GPa, respectively. Such gigapascal-level compressive stresses on silicon would generally require large hydraulic presses, whereas, here, the stress state is applied by the silica cladding alone.

We have compared the shift in the Raman spectra of the continuous silicon in our fibers to reference data for monocrystalline silicon (peak at ~517 cm^{-1} for silicon fiber core versus 520 cm^{-1} for monocrystalline Si). This shift is most likely associated to the polycrystallinity of the Si in our samples (37, 38). This shift in the Raman spectra is consistent with a previous study that showed the presence of nanometric-sized crystals on the surface of the core (14). An additional possible mechanism that could explain the shift is the presence of residual stresses resulting from thermal expansion mismatch between the silicon and the silica cladding, which occurs during cooling of the sample (39); this mechanism is undetectable by optical means (see *SI Evaluation of Stress in the Silica Cladding Surrounding the Sphere by Crossed Polarizers Technique*, Figs. S4–S7, and Table S2).

Large discrepancies between the photoelastic measurements, the Raman measurements, and the theoretical predictions still need to be accounted for. Our assumption is that the silicon spheres are much like the SiGe particles that solidify in a gradual manner, causing a "pressure focusing" effect, where the parts of the sphere solidifying last will likely be under higher compressive stress. The qualitative results on cracks surrounding SiGe particles are a clear indication of the nonuniform stress distribution, here with higher stresses on the "hot" side of the particles (see *SI Cracked Fiber Due to Stress Buildup* and Fig. S3). The photoelastic measurement only probes the stress at the boundary, whereas Raman measurements penetrate deeper in the sphere volume, the absorption depth in silicon of the 784-nm laser being 10 μm. From the previous argument, we then expect the associated measured pressures to be different. Future work is required to investigate pressures in the bulk of the spheres from simulation and experiments in pure silicon, as well as stress buildup in SiGe.

Discussion

To conclude, we have shown that the in-fiber breakup method is able to produce SiGe microparticles with a well-defined and controllable Janus morphology and Si microparticles with a high level of internal stress, due to the confined solidification in a silica cladding. The stresses developing from the anomalous expansion may constitute an interesting way to control the materials bandgap (12, 40). In addition, the Janus particles produced by slowly cooling SiGe droplets represent a main finding, with potential applications in components of traditional radio frequency circuitry or in quantum computing, if successfully scaled down to nanometric regime, which was shown to be potentially possible elsewhere (13–15). Furthermore, combining our ability to reorient particles through laser recrystallization with the idea of selective breakup (15), one can envision building in-fiber arrays of SiGe Janus particles connected across the junction to metallic buses, thus paving the way toward fully integrated in-fiber microelectronics.

Materials and Methods

Fiber Drawing. The fiber is fabricated using a thermal draw technique. A preform of 13-mm outer diameter and 1-mm core diameter was prepared, and then heated in a vertical furnace and drawn into a fiber. The powder was consolidated into a bulk in the furnace by feeding the preform at a rate of 1 mm/s at a temperature of 1,600 °C. In the last step, the fibers were fed at a rate of 1 mm/min and drawn at a speed 1 m/min, at a temperature of 2,050 °C, which resulted in a fiber with a 400-μm diameter.

Flame Breakup. The breakup of the SiGe core was performed using a hydrogen–oxygen torch with outlet diameter of 0.020" and by feeding the fiber through a flame resulting from 0.4 L/min flow of H_2 and 0.15 L/min flow of O_2 at an offset of 15 mm from the torch outlet.

The breakup of the Si core was achieved by feeding a fiber through the flame produced by a flow of 0.3 L/min and 0.2 L/min of H_2 and O_2, respectively.

Laser Recrystallization. Controlled recrystallization of spheres was obtained by feeding a fiber containing spheres through a laser heating setup. The fiber was heated locally by focusing an illumination from a fiber-coupled diode laser emitting light with a peak wavelength of 808 nm and a CO_2 laser. The diode was operated in a pulsed mode with a pulse rate of 5 kHz, controlled by a function generator, where the duty cycle was precisely tuned through a Labview program, to induce a controlled solidification rate.

For further details on the experimental methods, see *Supporting Information*.

ACKNOWLEDGMENTS. This research was supported, in part, by the US Army Research Office through the Institute for Soldier Nanotechnologies at Massachusetts Institute of Technology (MIT) (Contract W911NF-13-D-0001) and, in part, by the National Science Foundation through the MIT Center for Material Science and Engineering (Contract DMR-1419807).

1. Oldenburg SJ, Averitt RD, Westcott SL, Halas NJ (1998) Nanoengineering of optical resonances. *Chem Phys Lett* 288:243–247.
2. Ow H, et al. (2005) Bright and stable core-shell fluorescent silica nanoparticles. *Nano Lett* 5:113–117.
3. Lee J-H, et al. (2011) Exchange-coupled magnetic nanoparticles for efficient heat induction. *Nat Nanotechnol* 6:418–422.
4. Wang C, Yin H, Dai S, Sun S (2010) A general approach to noble metal-metal oxide dumbbell nanoparticles and their catalytic application for CO oxidation. *Chem Mater* 22:3277–3282.
5. McConnell MD, Kraeutler MJ, Yang S, Composto RJ (2010) Patchy and multiregion Janus particles with tunable optical properties. *Nano Lett* 10:603–609.
6. Ye S, Carroll RL (2010) Design and fabrication of bimetallic colloidal "Janus" particles. *ACS Appl Mater Interfaces* 2:616–620.
7. Yu H, et al. (2005) Dumbbell-like bifunctional Au-Fe3O4 nanoparticles. *Nano Lett* 5:379–382.
8. Simmchen J, et al. (2016) Topographical pathways guide chemical microswimmers. *Nat Commun* 7:10598.
9. Mehringer C, et al. (2014) Gas phase synthesis of anisotropic silicon germanium hybrid nanoparticles. *J Aerosol Sci* 67:119–130.
10. Welber B, Kim CK, Cardona M, Rodriguez S (1975) Dependence of the indirect energy gap of silicon on hydrostatic pressure. *Solid State Commun* 17:1021–1024.
11. Jacobsen RS, et al. (2006) Strained silicon as a new electro-optic material. *Nature* 441:199–202.
12. Sun Y, Thompson SE, Nishida T (2007) Physics of strain effects in semiconductors and metal-oxide-semiconductor field-effect transistors. *J Appl Phys* 101:1–22.
13. Kaufman JJ, et al. (2012) Structured spheres generated by an in-fibre fluid instability. *Nature* 487:463–467.
14. Gumennik A, et al. (2013) Silicon-in-silica spheres via axial thermal gradient in-fibre capillary instabilities. *Nat Commun* 4:2216.
15. Rein M, et al. (2016) Self-assembled fibre optoelectronics with discrete translational symmetry. *Nat Commun* 7:12807.
16. Olesinski RW, Abbaschian GJ (1984) The Ge-Si (Germanium-Silicon) system. *Bull. Alloy Phase Diagrams* 5:180–183.
17. Mogaddam NAP, et al. (2008) Phase separation in SiGe nanocrystals embedded in SiO2 matrix during high temperature annealing. *J Appl Phys* 104:124309.
18. Gotoh R, et al. (2012) Formation mechanism of cellular structures during unidirectional growth of binary semiconductor Si-rich SiGe materials. *Appl Phys Lett* 100:021903.
19. Littlejohns CG, et al. (2015) Next generation device grade silicon-germanium on insulator. *Sci Rep* 5:8288.
20. Coucheron DA, et al. (2016) Laser recrystallization and inscription of compositional microstructures in crystalline SiGe-core fibres. *Nat Commun* 7:13265.
21. Tiller W, Jackson K, Rutter J, Chalmers B (1953) The redistribution of solute atoms during the solidification of metals. *Acta Metall* 1:428–437.
22. Mullins WW, Sekerka RF (1964) Stability of a planar interface during solidification of a dilute binary alloy. *J Appl Phys* 35:444–451.
23. Koh H-YS, Chen S-L, Griffin PB, Plummer JD (2010) High quality single-crystal laterally graded SiGe on insulator by rapid melt growth. *Electrochem Solid-State Lett* 13:H281.
24. Yang X, et al. (2012) The critical growth velocity for planar-to-faceted interfaces transformation in SiGe crystals. *Appl Phys Lett* 100:141601.
25. Ballato J, et al. (2008) Silicon optical fiber. *Opt Express* 16:18675–18683.
26. Ballato J, et al. (2009) Glass-clad single-crystal germanium optical fiber. *Opt Express* 17:8029–8035.
27. Nagashio K, Jian Z, Kuribayashi K (2002) Direct observation of the crystal-growth transition in undercooled silicon. *Metall Mater Trans, A Phys Metall Mater Sci* 33:2947–2953.
28. Nagashio K, Okamoto H, Kuribayashi K, Jimbo I (2005) Fragmentation of faceted dendrite in solidification of undercooled B-doped Si melts. *Metall Mater Trans, A Phys Metall Mater Sci* 36A:3407–3413.
29. Dismukes JP, Yim WM (1974) A survey of interface stability criteria in the elemental alloy systems: Ge-Si, Bi-Sb, And Se-Te. *J Cryst Growth* 22:287–294.
30. Kostylev I, Woodacre JK, Lee YP, Klages P, Labrie D (2013) Melt zone growth of Ge-rich Ge1-xSix bulk crystals. *J Cryst Growth* 377:147–152.
31. Kürten M, Schilz J (1994) Czochralski growth of SitGe1-x single crystals. *J Cryst Growth* 139:1–5.
32. Dahlen A, Fattah A, Hanke G, Karthaus E (1994) Bridgman and Czochralski growth of Ge-Si alloy crystals. *Cryst Res Technol* 29:187–198.
33. Schilz J, Romanenko VN (1995) Bulk growth of silicon-germanium solid solutions. *J Mater Sci Mater Electron* 6:265–279.
34. Balluffi RW, Allen SM, Carter WC (2005) *Kinetics of Materials* (Wiley, New York).
35. Einhardt JÜR, Raith MM, Raase P, Reinhard J (2012) *Guide to Thin Section Microscopy* (Miner Soc Am, Chantilly, VA), 2nd Ed.
36. Sui Z, Burke HH, Herman IP (1993) Raman scattering in germanium-silicon alloys under hydrostatic pressure. *Phys Rev B Condens Matter* 48:2162–2168.
37. Campbell IH, Fauchet PM (1986) The effects of microcrystal size and shape on the one phonon Raman spectra of crystalline semiconductors. *Solid State Commun* 58:739–741.
38. Benrakkad MS, et al. (1995) Stress measurement by microRaman spectroscopy of polycrystalline silicon structures. *J Micromech Microeng* 5:132–135.
39. Fokine M, et al. (2017) Laser structuring, stress modification and Bragg grating inscription in silicon-core glass fibers. *Opt Mater Express* 7:85–92.
40. Healy N, et al. (2014) Extreme electronic bandgap modification in laser-crystallized silicon optical fibres. *Nat Mater* 13:1122–1127.
41. Brunco DP, Thompson MO, Hoglund DE, Aziz MJ, Gossmann HJ (1995) Germanium partitioning in silicon during rapid solidification. *J Appl Phys* 78:1575–1582.
42. Eshelby JD (1957) The determination of the elastic field of an ellipsoidal inclusion, and related problems. *Proc R Soc Sci* 241:376–396.
43. Vedam K, Davis TA (1967) Nonlinear variation of the refractive indices of α-quartz with pressure. *J Opt Soc Am* 57:1140–1145.

Supporting Information

Gumennik et al. 10.1073/pnas.1707778114

SI Analytical Derivation for the Ge Content Distribution in the Solid Phase

Let us denote the Ge content in the liquid and in the solid phase as ζ_L and ζ_S, respectively. Fig. S1*B* shows the relation $\zeta_S(\zeta_L)$ that is derived from the equilibrium phase diagram in Fig. S1*A*. Due to the instantaneous Ge content redistribution assumption, the fraction of the solid phase is a function of the Ge content in the liquid phase, $g=g(\zeta_L)$. Using the initial Ge content in the liquid phase, $\zeta_{L,0}$, the following equations can be obtained for the fraction of the solid phase and for the Ge mass conservation:

$$g(\zeta_L)=\int_{\zeta_S(\zeta_{L,0})}^{\zeta_S(\zeta_L)}\frac{dg}{d\zeta_{S'}}d\zeta_{S'} \qquad [S1]$$

$$\zeta_L(1-g(\zeta_L))+\int_{\zeta_S(\zeta_{L,0})}^{\zeta_S}\zeta_{S'}\frac{dg}{d\zeta_{S'}}d\zeta_{S'}=\zeta_{L,0}. \qquad [S2]$$

The first and the second terms on the left side of Eq. **S1** are the Ge content in the liquid and the solid phases, respectively. Differentiation of Eqs. **S1** and **S2** with respect to ζ_L, and substitution $dg/d\zeta_L$ obtained from Eq. **S1** in Eq. **S2**, results in the following equation:

$$\frac{dg}{d\zeta_L}=\frac{1-g(\zeta_L)}{\zeta_L-\zeta_S}. \qquad [S3]$$

Because $\zeta_S=\zeta_S(\zeta_L)$, Eq. **S3** can be solved for $g=g(\zeta_L)$, and its solution is described in Fig. S1*C*.

The relation between the melting temperature and the fraction of the solid phase, $T_M(g)$, depicted in Fig. S1*D* is extracted from $T_M(\zeta_L)$, shown in Fig. S1*A*, and $g(\zeta_L)$, shown in Fig. S1*B*. It is shown that the melting temperature drops as the solidification front propagates into the liquid phase.

To analytically derive the Ge content distribution in the solidified Ge-Si mixture droplet, it is necessary to add a geometrical relation between the solidification front and the solid fraction *g*. There are two main symmetries in our case: a radial symmetry, dominated by the temperature difference at the beginning of the isothermal stage between the droplet and its ambient due to recalescence, and an axial symmetry, dominated by the axial temperature gradient due to the laser induced heating. Here, we assume that the cooling rate is slow enough such that the solidification symmetry is dominated by the thermal gradient defined by the laser direction. As a result, in an axial symmetry for the solidification front propagation,

$$g\left(\frac{z}{r_0}\right)=\frac{1}{2}+\frac{3}{4}\left(\frac{z}{r_0}\right)-\frac{1}{4}\left(\frac{z}{r_0}\right)^3, \qquad [S4]$$

where z is the symmetry axis of the droplet such that the droplet center is at $z=0$, and r_0 is the droplet radius. Having the geometrical relation $g\left(\frac{z}{r_0}\right)$, the Ge content distribution in the solid phase can be calculated by

$$s\left(\frac{z}{r_0}\right)=\zeta_S\left\{\zeta_L\left[g\left(\frac{z}{r_0}\right)\right]\right\}. \qquad [S5]$$

Fig. S1*E* describes the analytically derived Ge content distribution in the solid phase, $\zeta_s\left(\frac{z}{r_0}\right)$. The analytical distribution is in good agreement with the experimental results.

SI Numerical Simulation of the Solidification Front Propagation Velocity

The modeled geometry includes a cylindrical silica fiber from $z=0$ to $z=L$, and half a silicon sphere of a radius r_S centered at the origin. The following heat equation is solved:

$$\rho C_P\frac{\partial T}{\partial t}-\nabla\cdot(k\nabla T)=Q,$$

where T is the temperature, t is the time, ρ, C_p, and k are the corresponding material density, heat capacity, and thermal conductivity, respectively, and $Q=Q(x,y,z,t)$ is a time-dependent heat source in the sphere. The heating of the Si sphere by a laser propagating in the $-y$ direction is modeled by a time-dependent heat source in the sphere. The heat source term is calculated by taking into account the laser radiation (in watts per square meter) absorption by the Si sphere. The radiation intensity on the sphere surface is approximated by $I_0(x,y,z,t)=P(t)/(\pi r_D^2)$ for $x^2+z^2<r_D^2$, and $I_0=0$ otherwise, where P is the diode laser power and r_D is its corresponding spot size radius. The y dependence of the laser radiation in the sphere is approximated by $dI/d\xi=-\alpha_{\mathrm{Si}}I(\xi)$, where $\xi=\sqrt{r_s^2-(x^2+z^2)}-y$, and the time-dependent heat source is approximated by $Q(x,y,z,t)=-dI/d\xi=\alpha_{\mathrm{Si}}I(\xi)=I_0(x,y,z,t)\alpha_{\mathrm{Si}}\exp(-\alpha_{\mathrm{Si}}\xi)$.

A symmetry boundary condition, $-\mathbf{n}\cdot\mathbf{q}=0$, is set for $z=0$, where $\mathbf{q}=k\nabla T$ is the heat flux and $\mathbf{n}$ is a normal vector to the boundary surface, and convective heat flux boundary conditions, $q_0=h\cdot(T_{\mathrm{ext}}-T)$, with $T_{\mathrm{ext}}=293.15$ [K], are set for $z=L$ and for $x^2+y^2=r_F^2$, with an axial and a radial convective heat flux coefficient, respectively. The initial conditions are determined by the solution for the corresponding stationary equation for $P=P_0$. In the initial condition, the entire sphere is in the liquid phase. As the laser intensity linearly decreases from $P=P_0$ at $t=0$ to $P=0$ for $t\geq t_{SD}$, the temperature in the sphere gradually drops below the silicon melting temperature of T_m, and the latent heat H_{Si} is extracted; the sphere gradually solidifies. The influence of the latent heat of fusion on the dynamics of the process is modeled in using the heat capacity formulation in which the heat capacity is effectively increased within a finite region of $\pm\Delta T_{L-S}/2$ near the melting temperature, T_M; the phase continuously changes from liquid to solid within this finite region. Table S1 summarizes the parameters that were used in the numerical simulation.

SI Homogeneous Solidification Scenario

Eshelby (42) has treated the general case of an ellipsoidal inhomogeneity of a material *S* embedded in an infinite matrix of a material *M*, and undergoing an arbitrary shape change. Here we treat a simplified case of a liquid sphere solidifying and expanding uniformly inside an infinite silica matrix. We consider a sphere of radius R_0 made of a material *S* in the liquid state, and embedded in an infinite matrix of a material *M* in the solid state. We assume that, before solidification, both the liquid and solid are stress-free. We consider now that the sphere homogeneously solidifies. In the process, the material acquires a purely dilatational stress-free

strain of $\epsilon^*_{ij} = (a/3)\delta_{ij}$, where $\alpha = \rho_{liquid}/\rho_{solid} - 1$ is the volume change upon solidification, and δ_{ij} is the Kronecker delta. We seek to determine the stress, strain, and displacement fields generated by the solidification process both in the sphere S and the matrix M.

For obvious symmetry arguments, we choose to work in spherical coordinates with the origin at the center of the sphere. We furthermore take the displacement field in both M and S to bear the form

$$\underline{u}^{S,M} = u^{S,M}(r)\,\underline{e_r}, \qquad \textbf{[S6]}$$

where $\underline{e_r}$ is the unit vector in the radial direction. Assuming small displacements, the strain tensors in M and S immediately derive from the above,

$$\varepsilon^{S,M}_{rr} = \frac{du^{S,M}}{dr} \qquad \textbf{[S7]}$$

$$\varepsilon^{S,M}_{\theta\theta} = \varepsilon^{S,M}_{\phi\phi} = \frac{u^{S,M}}{r}. \qquad \textbf{[S8]}$$

The total strain in M is purely elastic, whereas, in S, the total strain is the sum of the elastic strain and the transformation stress-free strain ϵ^*_{ij}. By assuming that both materials S and M behave as linearly elastic, we thus have

$$\varepsilon^M_{ij} = S^M_{ijkl}\sigma^M_{kl} \qquad \textbf{[S9]}$$

$$\varepsilon^S_{ij} = S^S_{ijkl}\sigma^S_{kl} + \epsilon^*_{ij}, \qquad \textbf{[S10]}$$

where $\sigma^{S,M}_{kl}$ are the stress tensors in both S and M, and $S^{S,M}_{ijkl}$ are the compliance tensors in both S and M. The above expressions contain implicit sums over k and l, according to the Einstein notation. Further considering that both materials S and M are mechanically isotropic and homogeneous, we can write the components of the stress tensors in terms of the materials bulk moduli and shear moduli, $K_{S,M}$ and $G_{S,M}$. They take the form

$$\sigma^M_{rr} = \left(K_M - \frac{2}{3}G_M\right)\left(\frac{du^M}{dr} + 2\frac{u^M}{r}\right) + 2G_M\frac{du^M}{dr} \qquad \textbf{[S11]}$$

$$\sigma^M_{\theta\theta} = \sigma^M_{\phi\phi} = \left(K_M - \frac{2}{3}G_M\right)\left(\frac{du^M}{dr} + 2\frac{u^M}{r}\right) + 2G_M\frac{u^M}{r} \qquad \textbf{[S12]}$$

$$\sigma^S_{rr} = \left(K_S - \frac{2}{3}G_S\right)\left(\frac{du^S}{dr} + 2\frac{u^S}{r}\right) + 2G_S\frac{du^S}{dr} - K_S\alpha \qquad \textbf{[S13]}$$

$$\sigma^S_{\theta\theta} = \sigma^S_{\phi\phi} = \left(K_S - \frac{2}{3}G_S\right)\left(\frac{du^S}{dr} + 2\frac{u^S}{r}\right) + 2G_S\frac{u^S}{r} - K_S\alpha. \qquad \textbf{[S14]}$$

We now proceed to applying the equilibrium condition in both M and S. In a static situation such as the one studied here, the equilibrium condition simply states that $\nabla\cdot\sigma = 0$ at any given point of the system. This yields

$$\frac{d\sigma^{S,M}_{rr}}{dr} + \frac{2\sigma^{S,M}_{rr} - \sigma^{S,M}_{\theta\theta} - \sigma^{S,M}_{\phi\phi}}{r} = 0. \qquad \textbf{[S15]}$$

Substituting in the previous expressions for stress components leads to a very simple differential equation on the displacement fields,

$$\frac{d}{dr}\left[\frac{du^{S,M}}{dr} + 2\frac{u^{S,M}}{r}\right] = 0. \qquad \textbf{[S16]}$$

Solving the previous equation exactly, one gets

$$u^{S,M}(r) = A_{S,M}r + \frac{B_{S,M}}{r^2}, \qquad \textbf{[S17]}$$

where $A_{S,M}$ and $B_{S,M}$ are integration constants. We note that B_S and A_M must equal zero to ensure a finite displacement field near the origin and zero stress at infinity, respectively.

The form of displacement field must also verify the continuity relations at the sphere/matrix interface.

$$\sigma^S_{rr}(r = R_0) = \sigma^M_{rr}(r = R_0) \qquad \textbf{[S18]}$$

$$u^S(r = R_0) = u^M(r = R_0). \qquad \textbf{[S19]}$$

Substituting in the form of the displacement fields in Eqs. **S18** and **S19**, one gets a simple linear system with solutions,

$$A_S = \frac{K_S}{3K_S + 4G_M}\alpha \qquad \textbf{[S20]}$$

$$B_M = \frac{K_S}{3K_S + 4G_M}\alpha {R_0}^3. \qquad \textbf{[S21]}$$

We thus get the exact stress, strain, and displacements fields in both the matrix M and the sphere S.

In M, $r > R_0$,

$$\varepsilon^M_{rr} = -\frac{2K_S}{3K_S + 4G_M}\alpha\frac{{R_0}^3}{r^3} \qquad \textbf{[S22]}$$

$$\varepsilon^M_{\theta\theta} = \varepsilon^M_{\phi\phi} = \frac{K_S}{3K_S + 4G_M}\alpha\frac{{R_0}^3}{r^3} \qquad \textbf{[S23]}$$

$$\sigma^M_{rr} = -\frac{4K_SG_M}{3K_S + 4G_M}\alpha\frac{{R_0}^3}{r^3} \qquad \textbf{[S24]}$$

$$\sigma^M_{\theta\theta} = \sigma^M_{\phi\phi} = \frac{2K_SG_M}{3K_S + 4G_M}\alpha\frac{{R_0}^3}{r^3}. \qquad \textbf{[S25]}$$

In S, $r \le R_0$,

$$\varepsilon^S_{rr} = \varepsilon^S_{\theta\theta} = \varepsilon^S_{\phi\phi} = \frac{K_S}{3K_S + 4G_M}\alpha \qquad \textbf{[S26]}$$

$$\sigma^S_{rr} = \sigma^S_{\theta\theta} = \sigma^S_{\phi\phi} = -\frac{4K_SG_M}{3K_S + 4G_M}\alpha. \qquad \textbf{[S27]}$$

We can thus express the hydrostatic pressure inside the sphere $P = -1/3\ tr\ \sigma^s$; we get

$$P = \frac{4K_SG_M}{3K_S + 4G_M}\alpha. \qquad \textbf{[S28]}$$

To give an intuitive picture, let's first take a look at two extreme cases: solidification in a free space and solidification in an ideally rigid matrix. Were it to solidify in free space, a sphere of initial volume V_{liquid} and radius R_0 would expand to occupy a larger spherical volume V_{solid} and radius R^*, without developing any stress (Fig. S2*A*). The nominal volume expansion upon

solidification α in that case is associated with a purely dilatational and homogeneous stress-free strain $\epsilon^*_{ij} = (\alpha/3)\delta_{ij}$, much like a thermal expansion strain. It is only when constrained by a matrix that elastic stresses and strains develop. For instance, we can consider the case of an infinitely rigid matrix. The sphere would then be exactly constrained to its original volume, and the total strain would thus be zero. The transformation strain ϵ^*_{ij} would then have to be balanced by an elastic strain of -ϵ^*_{ij}, hence developing a state of hydrostatic stress in the sphere of $\sigma_{ij} = -K_s\alpha\ \delta_{ij}$, where K_s is the bulk modulus of solid sphere material (Fig. S2*B*).

In the case of a finite rigidity matrix, the sphere of radius R_0 expands upon solidification to a sphere of radius R, with $R_0 \le R \le R^*$, and the strain and stress in the solid sphere and matrix will be the result of an interplay between the elastic properties of both materials (Fig. S2*D*). Assuming linear elastic behavior of both solid sphere and silica, we can write the total strain tensors in the form brought in Eqs. **S9** and **S10**. Solving for spherically symmetric displacement fields, and applying the equilibrium condition $\nabla \cdot \sigma = 0$, as well as continuity relations of radial stress and displacement at the sphere/matrix interface, we get Eqs. **S26**–**S28**. We conclude that the homogeneous expansion upon solidification of the sphere results in a state of homogeneous hydrostatic stress within the sphere, with a pressure $P = [4K_S G_M/(3K_S + 4G_M)]\alpha$, which equals 2.9 GPa for a silicon sphere in silica and 1.5 GPa for a germanium sphere in silica, assuming an expansion coefficient of 10.0% for silicon and 5.6% for germanium, a bulk moduli of 98 GPa for silicon and 75 GPa for germanium, and a shear modulus of silica 31 GPa. Taking the limiting cases of an infinitely rigid matrix ($G_M \to \infty$) and an infinitely compliant matrix ($G_M \to 0$) leads to results in agreement with intuition. We add that this result coincides with the general treatment of Eshelby's inhomogeneous inclusions (42) for the case of a sphere with transformational eigenstrain ϵ^*_{ij}.

SI Cracked Fiber Due to Stress Buildup

Fig. S3 shows a silica cladding fiber displaying cracks around the spheres.

SI Evaluation of Stress in the Silica Cladding Surrounding the Sphere by Crossed Polarizers Technique

We wish to rely on photoelastic effects to optically evaluate the stresses developing in the silica cladding around a solidified sphere. Here, we develop a model relating the stress in the silica cladding with the measured light intensity in a crossed polarizer configuration, to interpret our experimental data.

In photoelastic materials, there is a stress-induced birefringence causing the index of refraction to be different for light polarized along the different principal axes of the stress tensor. It is commonly accepted that this index of refraction difference is proportional to the difference in the principal components of the stress tensor, or similarly in a linear elastic solid to the difference in principal components of the strain tensor. In the silica cladding surrounding a solidified sphere, we thus have

$$\Delta n_{r,\theta}(r) = n_r - n_\theta = A\left[\varepsilon^M_{rr}(r) - \varepsilon^M_{\theta\theta}(r)\right] \qquad \textbf{[S29]}$$

$$\Delta n_{r,\phi}(r) = n_r - n_\phi = A\left[\varepsilon^M_{rr}(r) - \varepsilon^M_{\phi\phi}(r)\right] = \Delta n_{r,\theta} \qquad \textbf{[S30]}$$

$$n_r(r) = n_0 + A\varepsilon^M_{rr}(r), \quad n_\theta(r) = n_0 + A\varepsilon^M_{\theta\theta}(r), \qquad \textbf{[S31]}$$

where n_i indicates the index of refraction for light polarized in the i direction, and σ_{ii} is the principal component of stress in the i direction, which has been determined in *SI Analytical Derivation for the Ge Content Distribution in the Solid Phase* for the case of homogeneous solidification. The constant A is the so-called photoelastic constant of the material evaluated at $A = 1.2$ in silica (43), and $n_0 = 1.46$ is the stress-free refractive index of the material. Thus, the homogeneously solidified sphere induces a spherically symmetric birefringence in the silica cladding.

We consider now the situation in which we observe the sphere in the fiber through a microscope in transmission geometry. The natural coordinate system for the light propagation will be the cylindrical coordinate system $[\rho, \theta', z]$, where the z direction is aligned with the wavevector $\mathbf{k}$ of the propagating light, perpendicular to the fiber axis in the present configuration. Without loss of generality, we can choose the θ'-direction to be collinear with the θ-direction in the spherical coordinate system. We furthermore assume that the sample is placed between two crossed polarizers P and A, and that the fiber has a diameter $2R_{out}$. The polarizer P is aligned along the direction $\theta = 0$, and the analyzer A is aligned along the direction $\theta = \pi/2$. A schematic representation of the setup with definition of the axes can be found in Fig. S4. We make the first-order assumption that light propagates in a straight line along the z direction. In particular, we neglect the refraction at the air/cladding interface, and the bending of rays due to nonuniform refractive indices.

We can write the electric field at a point $[\rho, \theta, z]$ as

$$\underline{E}(\rho,\theta,z,t) = E\left(cos\ \theta\ \underline{e_\rho} - e^{i\Gamma(\rho,z)}\ sin\ \theta\ \underline{e_\theta}\right)e^{i(kz-\omega t)}, \qquad \textbf{[S32]}$$

where $\Gamma(\rho, z)$ is the phase shift between both components of the electric field due to the stress-induced birefringence at this point. Immediately after the polarizer P, the light is purely linearly polarized. As light progresses, both components of the light develop a mutual phase shift because of the stress-induced birefringence. The phase shift between both components of the electric field is governed by the differential equation

$$\frac{\partial\Gamma}{\partial z} = \frac{2\pi}{\lambda_0}\Delta n_{\rho,\theta}\ (\rho, z). \qquad \textbf{[S33]}$$

After passing through the whole sample, the electric field has a form

$$\underline{E}\ (\rho,\theta,t) = E\left(cos\ \theta\ \underline{e_\rho} - e^{i\Gamma(\rho)}\ sin\ \theta\ \underline{e_\theta}\right)e^{i(2kD-\omega t)}, \qquad \textbf{[S34]}$$

where $\Gamma(\rho)$ is the total phase shift between both components of the electric field, expressed as

$$\Gamma(\rho) = \int_{-R_{out}}^{R_{out}} \frac{\partial\Gamma}{\partial z}dz = \int_{-R_{out}}^{R_{out}} \frac{2\pi}{\lambda_0}\Delta n_{\rho,\theta}(\rho, z)\ dz. \qquad \textbf{[S35]}$$

Therefore, we need to determine $\Delta n_{\rho,\theta} = n_\rho - n_\theta$, the difference in index of refraction for light polarized in the ρ and in the θ direction. We can do so geometrically using the index ellipsoid method. At a given position $\underline{r}$ in spherical coordinates, the index ellipsoid will be a uniaxial ellipsoid with of its main axes aligned with the r direction with semiaxis $n_r(r)$, and another main axis chosen to be in the θ-direction with semiaxis $n_\theta(r)$, as represented in Fig. S5. For light propagating in the z direction, the ellipse of refractive indices that the light will "sense" is the intersection of the index ellipsoid with the (ρ, θ) plane at this point. This ellipse has one main axis along the θ-direction with semiaxis $n_\theta(r) = n_\theta(\rho, z)$, and another on along the ρ-direction with semiaxis $n_\rho(\rho, z)$. From this geometric construction, we get

$$n_\rho(\rho,z)=\frac{n_r(r)n_\theta(r)}{\sqrt{[n_\theta(r)cos\varphi]^2+[n_r(r)sin\varphi]^2}}=\frac{n_r(r)n_\theta(r)}{\sqrt{\left[n_\theta(r)\frac{\rho}{r}\right]^2+\left[n_r(r)\frac{z}{r}\right]^2}},$$

[S36]

where $r=\sqrt{\rho^2+z^2}$. Finally, we deduce the birefringence felt by the light propagating from P to A,

$$\Delta n(\rho,z)=n_\rho(\rho,z)-n_\theta(\rho,z)=n_\theta(r)\left[n_r(r)\sqrt{\frac{\rho^2+z^2}{n_\theta(r)^2\rho^2+n_r(r)^2z^2}}-1\right].$$

[S37]

Going back to Eq. **S35**, we can express the total phase shift between the two components of the light after propagation through the sample,

$$\Gamma(\rho)=\frac{2\pi}{\lambda_0}\int_{-R_{out}}^{R_{out}}\left\{\left(n_0+\frac{U}{2(\rho^2+z^2)^{3/2}}\right)\left[\left(n_0-\frac{U}{(\rho^2+z^2)^{3/2}}\right)\sqrt{\frac{\rho^2+z^2}{\left[n_0+\frac{U}{2(\rho^2+z^2)^{3/2}}\right]^2\rho^2+\left[n_0-\frac{U}{(\rho^2+z^2)^{3/2}}\right]^2z^2}}-1\right]\right\}dz,$$

[S38]

where $U=APR^3/2G_M$, with A as the photoelastic constant, P as the pressure inside the solidified sphere, and R as the radius of the sphere.

At the end of the optical path, the analyzer A lets through only the component that is parallel to $\theta=\pi/2$. Hence,

$$\underline{E_{out}}\,(\rho,\theta,t)=E\left(\cos\theta sin\theta-e^{i\Gamma(\rho)}\sin\theta cos\theta\right)e^{i\omega t}.$$

[S39]

Finally, the light intensity observed through the transmission microscope will be

$$I=\underline{E^*_{out}}\cdot\underline{E_{out}}=\frac{1}{2}E^2\sin^2\theta[1-\cos\Gamma(\rho)].$$

[S40]

The intensity I has fourfold symmetry in θ and a number of radial fringes correspondent to the magnitude of U, which depends both on the sphere size and on the pressure applied by it on the surrounding silica.

Fig. S6*A* depicts the intensity distribution for selected samples (highlighted in Table S2) as observed through a transmission optical microscope in crossed polarizer configuration, compared with the calculated intensity distributions based on the model in Eq. **S40**. Radial stress at the sphere surface is the fitting parameter tuned to obtain the right number of radial fringes for a given sphere size. Fig. S6*B* shows the upper limit of radial stress resulting from the same calculation for all of the samples in Table S2, compared with the radial stress at the sphere surface predicted by Eqs. **S26**–**S28**.

In the following paragraphs, we discuss how residual stresses arising from differential thermal expansion between the core and the cladding materials would be expressed in the continuous core region.

Assuming a stressed core, there should be cylindrically symmetrical stress in the cladding. This stress would have an opposite sign for axial direction compared with the radial direction: If, for instance, the core is compressed due to differential expansion upon cooling starting from the core solidification temperature to room temperature, then the cladding will be compressed radially, but tensed axially (along the core). This inevitably would express itself in cladding birefringence in the vicinity of the core, similarly to the spherical case discussed above. For cylindrical symmetry, the birefringence is cylindrically symmetric.

The polarizers' orientation described in Fig. 5 was chosen to coincide with the index ellipsoid axis, which explains the lack of transmission around the core, even in the presence of birefringence. More simply put, looking at the sphere on Fig. 5*B*, the dark lines in the fourfold symmetry coincide with the axis of symmetry of the continuous core.

An additional measurement at an arbitrary crossed polarizers' orientation, where the polarizers are not allied in parallel or in perpendicular to the core, is needed to support the absence of stress in the continuous core.

Such a measurement for the sample used for Raman measurement presented in Fig. 5 (35-μm-sized spheres) is shown in Fig. S7; the shown results supports the claim that the continuous core section is unstressed, to the extent detectable by optical means.

SI Materials and Methods

Fiber Drawing. The fiber is fabricated using a thermal draw technique. A preform (a macroscopic version of the fiber) is prepared, and then it is heated in the furnace and drawn into a fiber. In the first step, the pure Si or Ge powder or a mixture of Ge and Si powder with a certain mass ratio is placed inside a fused quartz tube. The tube has an inner diameter of 1 mm and an outer diameter of 6 mm. The tube is inserted into another larger tube with an inner diameter of 6 mm. To prevent any oxidization of the core material (Si, Ge, or Si_xGe_{1-x}) during the thermal draw, the core is capped on both ends with silica rods. The core region is pumped to vacuum, and the silica rods on both ends are sealed with the propane/oxygen flame. In this way, a preform of 13-mm outer diameter and 1-mm core is prepared. When the preform is ready, it is fed at a rate of 1 mm/s through a thermal draw furnace, which is heated to about 1,600 °C to melt the powder so that the core material is dense during the draw. In the last step, the preform is fed into the furnace at a rate of 1 mm/min and heated to about 2,000 °C; at this temperature, the preform components melt/soften and a fiber forms. The fibers are drawn at a speed of ∼1 m/min, which results in a fiber with a 400-μm diameter.

Flame Breakup. For the samples in Fig. 1, the breakup was performed using a hydrogen–oxygen torch with outlet diameter of 0.020" and by feeding the fiber through a flame resulting from 0.4 L/min flow of H_2 and 0.15 L/min flow of O_2 at an offset of 15 mm from the torch outlet. The core composition was $Si_{0.5}Ge_{0.5}$ in Fig. 1, and the feeding velocities through the flame were 2 μm/s. For the core of $Si_{0.75}Ge_{0.25}$ (Fig. 3*A*) and $Si_{0.95}Ge_{0.05}$ (Fig. 3*D*), the velocity of the feed was 10 μm/s, and the flame conditions were the same as for the Fig. 1 spheres.

The spheres used for birefringence measurements in Fig. 5*C* were made by feeding a fiber through the flame produced by a flow of 0.3 L/min and 0.2 L/min of H_2 and O_2, respectively. The fiber was held at the distance of 6 mm from the orifice of the torch. The feed speed through the flame was 20 μm/s. The sphere on Fig. 5*D* is made by feeding a fiber through the flame produced by a flow of 0.55 L/m and 0.22 L/m of H_2 and O_2, respectively. The fiber was held at a distance of 6 mm from the orifice of the torch. The feed speed through the flame was 10 μm/s.

SEM Sample Preparation, Imaging, and EDS Image Analysis. Fibers containing spheres that underwent different thermal processing treatments (either flame or laser breakup) were encapsulated in a cold mounting epoxy (Struers Epofix) and polished until the spheres were exposed at the surface of the sample, approximately at the midplane of the spheres. Samples were gold-sputtered before

imaging. SEM micrographs (Zeiss Merlin) in backscattered mode and EDS analysis (Octane Super; EDAX) were obtained with the polished samples. The solid light green/red lines in Fig. 1*F* correspond to a single pixel linescan, that is, a 0.7-μm-wide analysis area. The solid dark green/red lines correspond to the same linescan with a 14.7-μm-wide analysis area, and are calculated by having the 2D image filtered using a 10-pixel radius disk [see the function fspecial('disk',10) in MATLAB].

Laser Recrystallization. Controlled recrystallization of spheres was obtained by feeding a fiber containing spheres through a laser heating setup. The fiber was heated locally by focusing an illumination (spot size of ~50 μm, power 2 W) from a fiber-coupled diode laser (L4-2495; JDSU) emitting light with a peak wavelength of 808 nm. The diode was operated in a pulsed mode with a pulse rate of 5 kHz, controlled by a function generator (Tektronix AFG3252), where the duty cycle was precisely tuned through a Labview program, to induce a controlled solidification rate.

Additionally, the silica cladding of the fibers was locally preheated by focusing the radiation of a pulsed CO_2 laser (DEOS GEM-25L; Coherent), controlled through the previously mentioned function generator (pulse rate of 5 kHz). The beam was split into two for even heating of the fiber from two opposite directions. Each delivered beam was focused with a cylindrical lens to a spot size of ~3×1 mm^2 with ~2 W average power.

The positioning of the fiber was achieved by moving with a motorized stepper actuator (ZFS25B; Thorlabs) and rotating with a motorized rotary stage (RT-2D-10-S; Newark Systems) the fiber in the setup, while observing the location of the sphere relative to the laser beams, through a custom-built microscope.

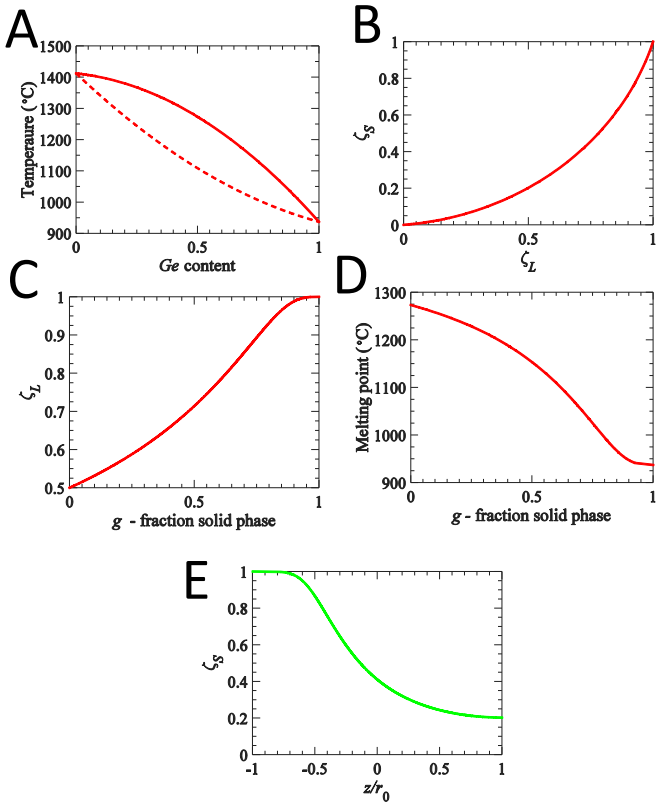

Fig. S1. Analytical derivation results for the Ge content distribution in the solid phase. (*A*) The Ge-Si liquidus (solid) and solidus (dashed) lines in accordance with the equilibrium phase diagram from ref. 16. (*B*) The Ge content in the solidified phase, ζ_s, as a function of the Ge content in the liquid phase ζ_L. (*C*) The fraction of the solid phase as a function of the Ge content in the liquid phase. (*D*) The derived melting point of the remaining liquid phase in the droplet as a function of the fraction solid phase, *g*. (*E*) The Ge content distribution in the solid phase as a function of z/r_0, analytically derived assuming axial symmetry solidification; *z* is the symmetry axis of the droplet such that the droplet center is at $z = 0$, and r_0 is the droplet radius.

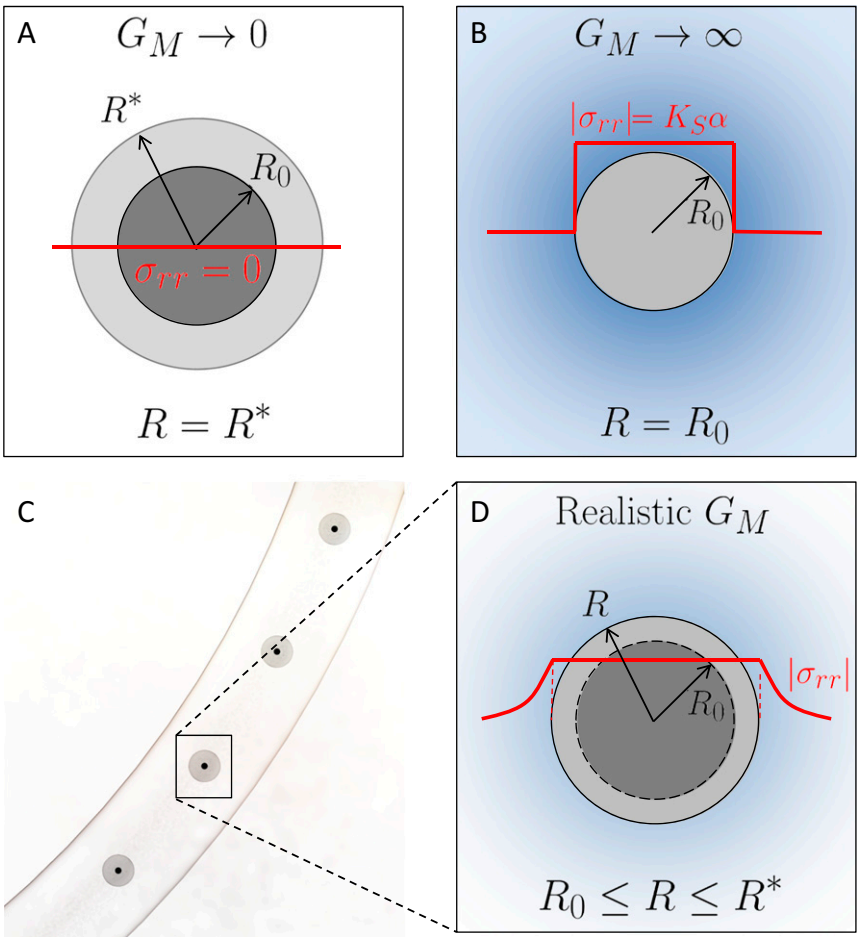

Fig. S2. Schematic representation of volume expansion and stresses in spheres homogeneously solidifying in different matrices. The dark gray circles indicate the reference liquid state, and the light gray circles represent the final solid state; G_M denotes the shear modulus of the matrix. (*A* and *B*) Limit cases, with (*A*) solidification in free space, or infinitely compliant matrix, and (*B*) solidification in an infinitely rigid matrix. (*D*) A more realistic case of solidification in a finite compliance matrix. (*C*) A sketch of a silica fiber containing four pressurized solid spheres.

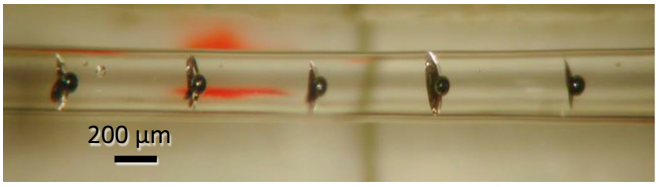

Fig. S3. Photograph of a silica cladding fiber displaying cracks around $Si_{0.5}Ge_{0.5}$ spheres, indicating a pressure buildup due to anomalous expansion of the alloy upon solidification.

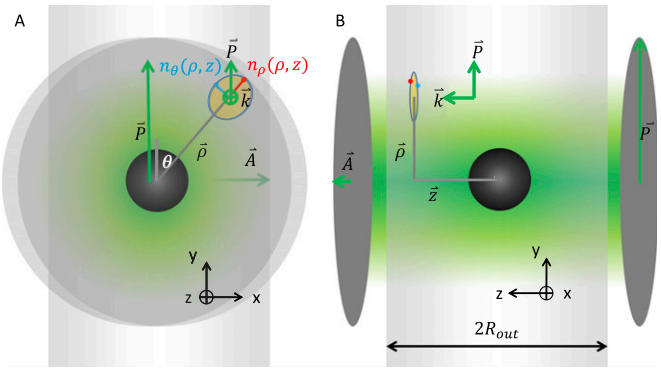

Fig. S4. The polarization evolution of the light propagating around the sphere in cross-polarized setup. (*A*) View normal to the fiber axis *z*. (*B*) View on to the side of the fiber, normal to the radial direction, *x* or ρ.

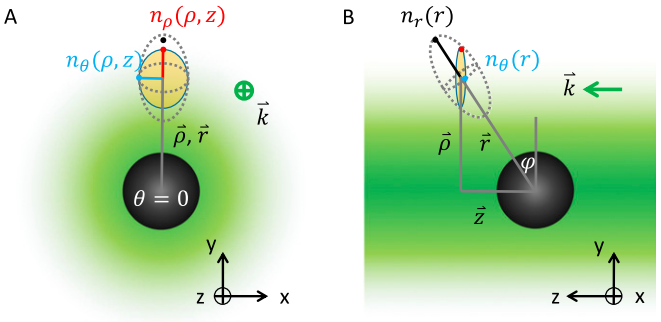

Fig. S5. The birefringence felt by the light propagating around the sphere at arbitrary point. (*A*) View normal to the fiber axis *z*. (*B*) View on to the side of the fiber, normal to the radial direction, *x* or ρ.

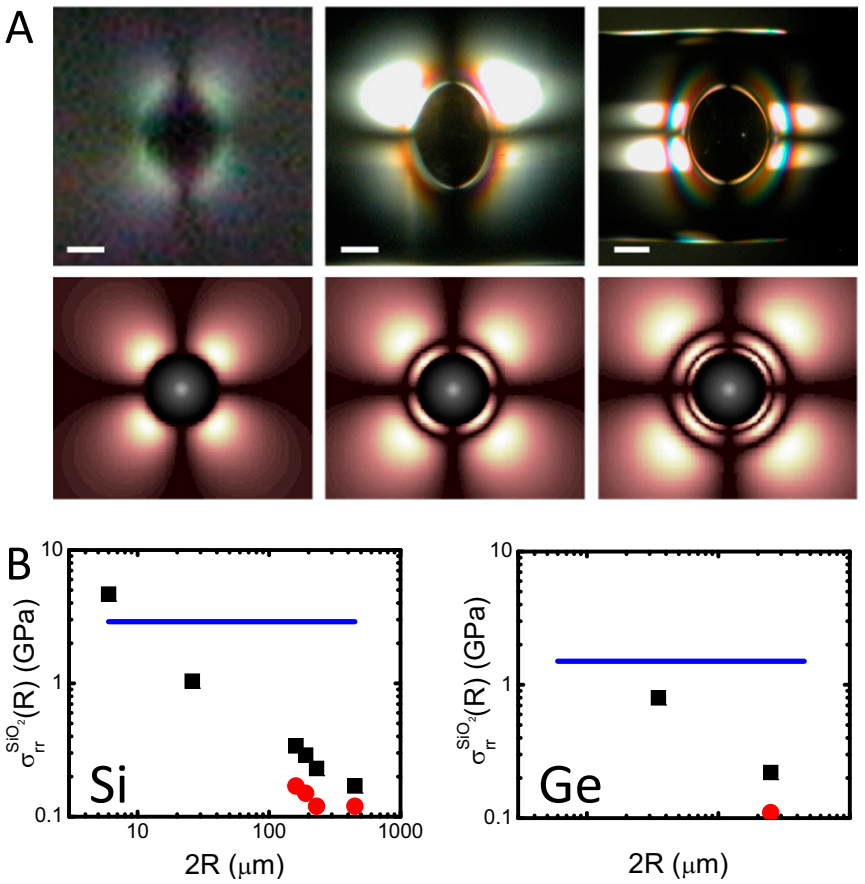

Fig. S6. Stress evaluation in the cladding of the sphere through the birefringence measurement. (*A*) Intensity distribution for selected samples with (from left to right) $R = 3$ μm (scale bar, 3 μm), $R = 95$ μm (scale bar, 100 μm), and $R = 225$ μm (scale bar, 200 μm), as is observed through (*Top*) a transmission optical microscope in crossed polarizers configuration compared with (*Bottom*) the calculated intensity distributions based on model in *SI Homogeneous Solidification Scenario*; the upper limit for the radial stresses is determined based on the fact that, for the sphere with $R = 3$ μm, the number of fringes $N \leq 1$; for $R = 95$ μm, $N \leq 2$; and, for $R = 225$ μm, $N \leq 3$. The ellipsoidal shape of the spheres in *Top* is due to the refraction of light as it propagates through the cylindrical cladding; it is thus a pure artifact of the imaging process. (*B*) Upper limit (black square) and lower limit (red circle) of radial stresses (bars) for Si (*Left*) and Ge (*Right*) samples in Table S2, compared with the radial stresses at the sphere surface predicted by Eq. **S28** (solid line). For the spheres for which no lower limit is represented, the lower limit is 0 GPa.

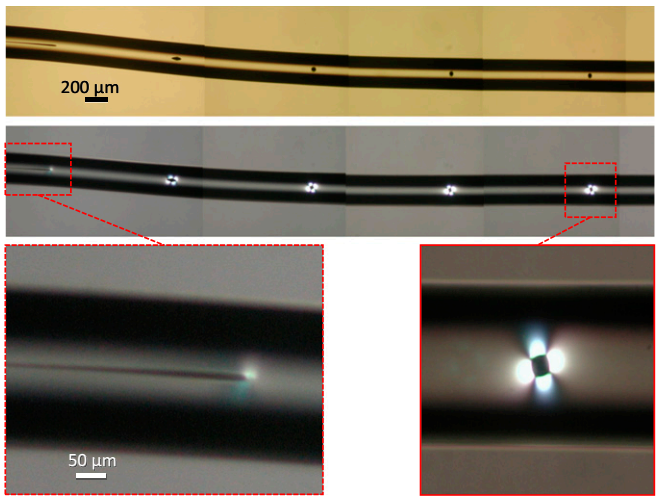

Fig. S7. Cross-polarizer imaging of the 35-μm-sized spheres sample used for Raman measurements in Fig. 5*F* at an arbitrary crossed polarizers' orientation, where the polarizers are not aligned in parallel or perpendicular to the core. These findings support the absence of stress in the continuous core.

Table S1. List of parameters used in the numerical simulation results

Parameter	Expression	Value
Sphere radius, μm	r_S	50
Fiber radius, μm	r_F	225
Half the modeled section length, μm	L	2,500
Diode-laser spot size radius, μm	r_D	25
Initial diode-laser power, W	P_0	2
Absorption coefficient of Si at 808 nm, $L{\cdot}\mu m^{-1}$	α_{Si}	0.079
Density of Si in the liquid phase, $kg{\cdot}cm^{-3}$	$\rho_{Si,L}$	2,530
Density of Si in the solid phase, $kg{\cdot}cm^{-3}$	$\rho_{Si,S}$	2,311
Density of silica, $kg{\cdot}cm^{-3}$	ρ_{silica}	2,218
Heat capacity of Si in the liquid phase, $J{\cdot}kg^{-1}{\cdot}K^{-1}$	$C_{Si,L}$	909
Heat capacity of Si in the solid phase, $J{\cdot}kg^{-1}{\cdot}K^{-1}$	$C_{Si,S}$	995
Heat capacity of silica, $J{\cdot}kg^{-1}{\cdot}K^{-1}$	C_{silica}	1,350
Thermal conductivity of Si in the liquid phase, $W{\cdot}m^{-1}{\cdot}K^{-1}$	$k_{Si,L}$	59
Thermal conductivity of Si in the solid phase, $W{\cdot}m^{-1}{\cdot}K^{-1}$	$k_{Si,S}$	22
Thermal conductivity of silica, $W{\cdot}m^{-1}{\cdot}K^{-1}$	k_{silica}	10
Silicon melting temperature, K	T_m	1,687
Silicon latent heat, $J{\cdot}kg^{-1}$	H_{Si}	$1.8{\cdot}10^6$
Transition interval between the liquid phase and the solid phase, K	ΔT_{L-S}	5
Axial convective heat flux coefficient, $W{\cdot}m^{-1}{\cdot}K^{-1}$	h_{axial}	15,000
Radial convective heat flux coefficient, $W{\cdot}m^{-1}{\cdot}K^{-1}$	h_{radial}	300

Table S2. Breakup conditions and resulting sphere sizes

Core material	Fiber diameter, μm	Core diameter, μm	H flow, L/min	O flow, L/min	Distance from the torch outlet to the fiber, mm	Feed speed, μm/s	Sphere diameter, μm
Si	**1,230**	**183**	**0.55**	**0.23**	**6**	**10**	**450**
Si	670	82	0.36	0.13	6	10	230
Si	**760**	**63**	**0.41**	**0.15**	**6**	**10**	**190**
Si	1,670	45	0.52	0.2	6	10	160
Si	280	4	0.3	0.2	10	20	26
Si	**56**	**0.8**	**0.3**	**0.2**	**10**	**20**	**6**
Si	280	4	1.0 ± 0.2	0	54 ± 2	10	35.0 ± 0.4
Ge	480	111	0.43	0.15	10	10	250
Ge	700	10	0.34	0.11	10	10	35

The boldfaced lines correspond to the samples used for visual representation of stress evaluation by birefringence measurements in Fig. S6*A*.